Complex-valued acquisition of the diffraction imaging by incoherent quasimonochromatic light without a support constraint

Minghui Zhang,* Jianfei Xu, and Xianfu Wang
School of Physics and Material Science, Anhui University, No. 3 Feixi Road, Hefei 230039, People's Republic of China

Qing Wei†
Key Laboratory for Quantum Optics and Center for Cold Atom Physics, Shanghai Institute of Optics and Fine Mechanics, Chinese Academy of Science, P.O. Box 800-211, Shanghai 201800, People's Republic of China
(Received 7 June 2010; revised manuscript received 31 August 2010; published 27 October 2010)

A scheme for complex-valued acquisition of the diffraction imaging with quasimonochromatic incoherent light is theoretically proposed. The main idea is to project the real and the imaginary parts of a Fraunhofer diffraction field on intensity distributions, respectively, with the use of a $\pi/2$ phase-changing plate. The whole procedure is iterative algorithm free and needs no *a priori* knowledge of an arbitrary object. A numerical experiment and a quantitative confirmation are also given. To our knowledge, it was the first physical proposal for the complex-valued acquisition of a diffraction imaging by two-dimensional coherent patterns with thermal illumination.

DOI: 10.1103/PhysRevA.82.043839 PACS number(s): 42.25.Hz, 42.25.Kb, 42.30.Rx

I. INTRODUCTION

Based on the fact that Fourier transform keeps unitary relations between the real and the reciprocal spaces (Fourier space), the obtained coherent Fraunhofer diffraction patterns are being called Fourier-transform *imaging*. To sustain the unitary quality, great effort has been employed with the use of iterative algorithms [1–3] to phase the modulus of diffraction patterns. The applications of this procedure (e.g., Ref. [4]) are essential for the coherent x-ray diffraction imaging [1,5–11] and have been extended from x-ray crystallography for the imaging of noncrystalline materials and single cells as reviewed in Ref. [12].

In general, a coherent source or a periodic object is needed to obtain the diffraction patterns. As in the situation where they were both unavailable, the technique of coincident imaging (also known as correlation imaging, ghost imaging, etc.), has recently been suggested as a substitute (e.g., Refs. [13–17]). The phaseless patterns obtained in this way were reversed to an amplitude only, and not long ago, a pure-phased object had been reported [13]. In the works of Refs. [18] and [19], the authors showed that a ghost-imaging scheme retrieves amplitude transmittance of objects rather than the intensity transmittance as the Hanbury-Brown–Twiss-type imaging scheme does. Based on this feature, Ying *et al.* realized the complex retrieval of an object with discrete phase variables [20] combined with the oversampling method [21] and the iterative algorithm [1–3]. Yet, ways mentioned previously, to recover the phase encoded in the diffraction pattern, have to rely on a support constraint of the objects more (e.g., Ref. [2]) or less (e.g., Ref. [22]). Otherwise, ambiguity would arise. In 2006, the authors of Ref. [23] reported an experiment for complex-valued retrieval of a diffraction field with a pseudothermal source using a ghost diffraction scheme. In their work, each pixel of the diffraction field needed a set of sinusoidal patterns to determine both the amplitude and the phase.

In this paper, we theoretically propose a scheme for complex-valued acquisition of a diffraction field with a type of Fourier transform. The main idea is to project the real and the imaginary parts, respectively, of the field on intensity distributions. The whole procedure to sustain the unity is iterative algorithm free and needs no assumptions on the to-be-resolved object. The diffraction patterns are to be obtained under spatially incoherent illumination. In addition, unlike the coincident imaging, the coherent patterns are carried out by the intensity itself rather than by the correlation function of intensity fluctuations.

We propose the experimental setup in Sec. II and the acquisition procedures in Sec. III. After that, their theoretical explanations are given in Sec. IV. Then, as an example, a numerical experiment is demonstrated in Sec. V. For a rigorous confirmation, the object and the imaging are compared quantitatively in Sec. VI. Finally, the paper is summarized in Sec. VII.

II. PROPOSED SCHEME

The proposed scheme is shown in Fig. 1(a). It might be similar to the Mach-Zehnder interferometer at first glance. But after modification, its mechanism will be quite different from its original purpose [24] (p. 348). Fields from the thermal source are split by a 50-50 beam splitter BS_1 to form a two-arm optical system with equal optical distance from source plane x to detection planes η_2 and η_1, where intensity information would be recorded. At the cross section of both arms before η_2 and η_1, the other 50-50 beam splitter BS_2 would be placed. When a situation needs to introduce a phase-shift factor of j, a $\pi/2$ phase-changing plate J would be inserted into the lower part of the system.

Note there are two modifications that lead the total scheme to differ mainly from the Mach-Zehnder

*zmh@ahu.edu.cn
†qingw@siom.ac.cn

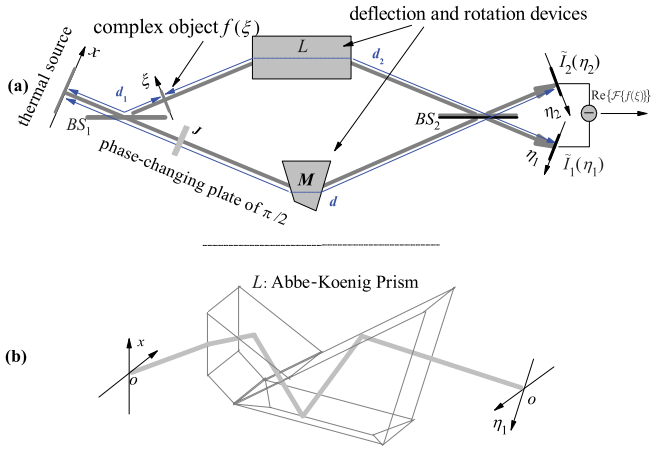

FIG. 1. (Color online) (a) The proposed scheme for the setup. There are two modifications that lead the total scheme to differ mainly from the Mach-Zehnder interferometer. One is that it uses deflection and rotation devices rather than plane mirrors to guide the optical path in both upper and lower parts, shown as L and M. Among them, L can be an Abbe-Koenig prism, and M can be an ordinary prismatic lens. The other is that the half-wave loss of reflection occurs only on the upper side of BS_2's surface, while it occurs (or does not occur) on both sides of BS_1; (b) Abbe-Koenig prism, an example of the deflection and rotation device L in (a).

interferometer. The first one is that it uses deflection and rotation devices (L and M) rather than plane mirrors, to guide the optical path. Among them, for example, L can be an Abbe-Koenig prism [Fig. 1(b)], and M can be an ordinary prismatic lens. The second modification is that the half-wave loss of reflection manages to occur only on the upper side of BS_2's surface, while it occurs (or does not occur) on both sides of BS_1.

For simplicity, we use the same letter to describe both the planes and the coordinate variables on them in the following paragraphs. The object with complex transmittance of $f(\xi)$ is placed at plane ξ. In one optical path, the optical distance from plane x to plane ξ, and from plane ξ to plane η_1 are d_1 and d_2, respectively; in the other optical path, the optical distance from plane x to plane η_2 is d. The setup is shown in Fig. 1(a). The equal optical length of the two arms requires that

$$d = d_1 + d_2. \tag{1}$$

III. ACQUISITION PROCEDURE

The object with complex transmittance of $f(\xi)$ is placed at plane ξ as Fig. 1(a) shows. Before and after the phase-changing plate J is inserted, the intensity distributions $\tilde{I}_k(\eta_k)$ and $\tilde{I}'_k(\eta_k)$ in both arms would be recorded. The subscripts $k = 1,2$, refer to planes η_1 and η_2, respectively. Then, the complex Fourier transform of the object's transmittance can simply be concluded as equation,

$$\mathcal{F}\{f(\xi)\} = \mathfrak{F}\left(\frac{2\eta}{\lambda d_2}\right) \propto \frac{\tilde{I}'_1(\eta_1) - \tilde{I}'_2(\eta_2)}{2} + j\frac{\tilde{I}_2(\eta_2) - \tilde{I}_1(\eta_1)}{2} \tag{2}$$

gives.

IV. THEORY

We assume the source is quasimonochromatic with a mean wavelength of λ. For simplicity, only one transverse dimension is considered, although the generalization for two transverse dimensions is straightforward. To illustrate the procedure clearly, we first suppose that we had not facilitated the beam splitter BS_2 and J in Fig. 1. Under the narrow-band condition, the amplitude impulse response is still valid for instantaneous values of field strength, so the E_2 on η_2 and the E_1 on η_1 at time t fulfill [25]

$$E_2(\eta_2,t) = \sqrt{\frac{e^{jkd}}{j\lambda d}} \int_x E_0(x,t-\tau) e^{jk[(\eta_2 - x)^2/2d]}\, dx, \tag{3}$$

and

$$E_1(\eta_1,t) = \sqrt{\frac{e^{jkd_2}}{j\lambda d_2}} \int_\xi \left[\sqrt{\frac{e^{jkd_1}}{j\lambda d_1}} \int_x E_0(x',t-\tau) \times e^{jk[(\xi - x')^2/2d_1]}\, dx' \right] f(\xi) e^{jk[(\eta_1 - \xi)^2/2d_2]}\, d\xi, \tag{4}$$

respectively, under the Fresnel approximation. In the equations, E_0 means field strength in the source plane, and τ refers to the time interval during which the optical fields propagate from source to detection planes. We have to make it clear here, that the transmittance function of the deflection and rotation devices, L and M did not appear in Eqs. (3) and (4) because they only introduce a phase factor of a plane wave to the detection areas, so the setup can be arranged to cancel them just by adjusting the tilt angles of planes η_1 and η_2.

Suppose that the thermal source is totally spatially incoherent [26] with evenly distributed intensity I_0. This assumption equals

$$\langle E_0^*(x,t-\tau) E(x',t-\tau) \rangle = I_0 \delta(x - x'), \tag{5}$$

in which $\langle \cdots \rangle$ means the time average during the detector integration period. As for a thermal light, which was an ensemble of a large number of independent radiating units and in which each individual radiates by spontaneous radiation randomly and independently, the model can approximately be viewed as totally chaotic in spatial. So, the Dirac-δ-function form of Eq. (5) can be thought of as appropriate to describe the most laboratory-available thermal source. If the source surface is large enough, the mutual intensity between planes η_1 and η_2 can be derived from Eqs. (1) to (5) as

$$\begin{aligned} &\langle E_2^*(\eta_2,t) E_1(\eta_1,t) \rangle \\ &= j\frac{I_0}{\lambda d_2} e^{jk[(\eta_1^2 - \eta_2^2)/2d_2]} \int_\xi f(\xi) e^{-j2\pi[(\eta_1 - \eta_2)/\lambda d_2]\xi}\, d\xi \\ &= j\frac{I_0}{\lambda d_2} e^{jk[(\eta_1^2 - \eta_2^2)/2d_2]} \mathcal{F}\{f(\xi)\}|_{[(\eta_1 - \eta_2)/\lambda d_2]} \\ &\propto j\mathfrak{F}\left(\frac{\eta_1 - \eta_2}{\lambda d_2}\right). \end{aligned} \tag{6}$$

Where $\mathfrak{F}(\cdots)$ refers to $\mathcal{F}\{f(\xi)\}$, the Fourier transform of $f(\xi)$.

Then, with the beam splitter BS_2 facilitated, the instantaneous value of fields in planes η_1 and η_2 turn out to become (we use tildes to denote situations when BS_2 is facilitated):

$$\widetilde{E}_2(\eta_2,t) = \frac{1}{\sqrt{2}}\left[E_2(\eta_2,t) - E_1(\eta_1,t)\right], \tag{7}$$

and

$$\widetilde{E}_1(\eta_1,t) = \frac{1}{\sqrt{2}}\left[E_2(\eta_2,t) + E_1(\eta_1,t)\right]. \tag{8}$$

On the right-hand sides of Eqs. (7) and (8), the two $E_1(\eta_1,t)$'s with opposite signs, due to half-wave loss, only occur on the upper side of BS_2.

As we know, any recorded intensity information must be a time average of the instantaneous intensity due to the fact that the detector integration time is usually extremely long compared with the coherent time of the optical field (Ref. [25], p. 132). Hence, the corresponding intensity distributions recorded on planes η_1 and η_2 are as

$$\widetilde{I}_2(\eta_2) = \langle \widetilde{E}_2^*(\eta_2,t)\widetilde{E}_2(\eta_2,t)\rangle = \tfrac{1}{2}[\langle |E_2(\eta_2,t)|^2\rangle - 2\,\mathrm{Re}\,\langle E_2^*(\eta_2,t)E_1(\eta_1,t)\rangle + \langle |E_1(\eta_1,t)|^2\rangle], \tag{9}$$

and

$$\widetilde{I}_1(\eta_1) = \langle \widetilde{E}_1^{\star}(\eta_1,t)\widetilde{E}_1(\eta_1,t)\rangle = \tfrac{1}{2}[\langle |E_2(\eta_2,t)|^2\rangle + 2\,\mathrm{Re}\,\langle E_2^*(\eta_2,t)E_1(\eta_1,t)\rangle + \langle |E_1(\eta_1,t)|^2\rangle] \tag{10}$$

as represented. From the two preceding equations, we can see that the real part of Eq. (6) is being embedded in the intensity information on both plane η_1 and plane η_2 and can be extracted by subtracting the two equal backgrounds by means of

$$\mathrm{Re}\,\langle E_2^*(\eta_2,t)E_1(\eta_1,t)\rangle = \frac{\widetilde{I}_1(\eta_1) - \widetilde{I}_2(\eta_2)}{2}. \tag{11}$$

Furthermore, the linearity of Eq. (6) indicates that, if a phase shift of φ is introduced in the lower part of the scheme shown as Fig. 1, consequently, a phase factor of $e^{-j\varphi}$ would be multiplied on the right-hand side of the equation. Following this thought, if we inserted a phase-changing plate J into the lower part of the system to introduce a phase shift of $\pi/2$, consequently, the complex vector, which stands for Eq. (6), would rotate at an angle of $-\pi/2$. Hence, the imaginary part of Eq. (6) can also be retrieved in a way similar to Eq. (11) as

$$\mathrm{Im}\,\langle E_2^*(\eta_2,t)E_1(\eta_1,t)\rangle = \frac{\widetilde{I}_1'(\eta_1) - \widetilde{I}_2'(\eta_2)}{2} \tag{12}$$

gives. Note that we use deflection and rotation devices (L and M) instead of plane mirrors, to guide the optical path. This arrangement leads to a centrosymmetry between coordinates in planes η_1 and η_2 [i.e., $\eta_1 = -\eta_2(\triangleq \eta)$], so,

$$\eta_1 - \eta_2 = 2\eta. \tag{13}$$

Comparing Eqs. (6) and (11)–(13), we see the complex-valued acquisition of an object's diffraction imaging with this type of Fourier transform can be achieved by the proposed scheme; and, thus, the procedure can be written in one equation as Eq. (2) presented.

V. A NUMERICAL EXPERIMENT

In Sec. IV, we have theoretically analyzed that the method worked with objects so long as their Fourier transform or generalized Fourier transform existed, and no other requirement was needed. So, the suggestion fit for those arbitrary objects rather than for a special one. Without sacrificing the generality, we conceived an object of a complex-valued transmittance:

$$f(\xi) = \left\{(1+\cos\,0.05\xi) + j\left[\mathrm{rect}\left(\frac{\xi+150}{105}\right) + \mathrm{rect}\left(\frac{\xi-150}{105}\right)\right]\right\}\mathrm{rect}\left(\frac{\xi}{1000}\right), \tag{14}$$

in which space parameters in plane ξ use micrometer (μm) units. It is well known that if this object was supposed to be transformed by a so-called 2-f system (or f-f system) [27] with $\lambda = 0.532\ \mu$m and $f = 75\,000\ \mu$m, the real and the imaginary parts of its Fourier-transform field as a function of space coordinates η would be

$$\mathrm{Re}\,\{\mathcal{F}\{f(\xi)\}\} = 500\,\mathrm{sinc}\left[1000\left(\frac{\eta}{\lambda f} + \frac{0.05}{2\pi}\right)\right] + 1000\,\mathrm{sinc}\left(1000\frac{\eta}{\lambda f}\right) + 500\,\mathrm{sinc}\left[1000\left(\frac{\eta}{\lambda f} - \frac{0.05}{2\pi}\right)\right], \tag{15}$$

and

$$\mathrm{Im}\,\{\mathcal{F}\{f(\xi)\}\} = 210\,\mathrm{sinc}\left(105\frac{\eta}{\lambda f}\right)\cos\left(300\pi\frac{\eta}{\lambda f}\right), \tag{16}$$

as Fig. 2 shows. Equations (15) and (16) were generally recognized as the object's function described in the Fourier space.

Based on the theory of statistical optics, we numerically simulated the dynamic process of the whole acquisition procedure under the setup scheme of Fig. 1. We summarized the detailed description here, although a similar model had been described in Ref. [28]. The random process of the thermal light was simulated as an ensemble $\mathbf{E_0}$ of a set of time series. Among $\mathbf{E_0}$, each sample function $E_0(k,t) = a(k,t)e^{j\theta(k,t)}$ stands for the complex-field strength of the kth radiating unit on the source plane x at time t. As every radiating unit is independent, this model will be in accord with Eq. (5) automatically. The fluctuations for the thermal source fulfill the complex circular Gaussian random process with zero mean; this feature is simulated by commanding the amplitude $a(k,t)$ to obey Rayleigh distribution in $[0,+\infty)$ and the phase $\theta(k,t)$ to obey uniform distribution in $[0,2\pi)$ [26]. The propagation of the fields was simulated according to Fresnel diffraction theory [25]. In the numerical experiment, the mean wavelength of the thermal light was selected to be $\lambda = 0.532\ \mu$m; the source's linear dimension was set to $l = 1$ cm. For the setup, d_1, d_2, and d are set to 6, 7.5, and 13.5 cm. According to the van Cittert-Zernike theorem, the liner dimension of the coherent area will be $\Delta x \approx \lambda\frac{d_1}{l} = 0.532\ \mu\mathrm{m} \times \frac{60\ \mathrm{mm}}{1\ \mathrm{cm}} = 3.19\ \mu$m, which was larger than zero and much smaller than the feature size of 105 μm of the object. Hence, Eq. (5) is a good approximation. With ensembles of instantaneous values of $\widetilde{E}_2(\eta_2,t_n)$ and $\widetilde{E}_1(\eta_1,t_n)$ $(n = 1,2,\ldots,N)$ generated

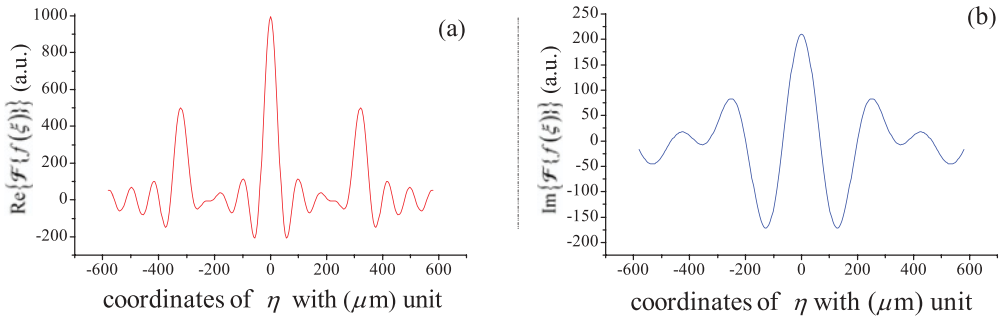

FIG. 2. (Color online) The (a) real [Eq. (15)] and (b) imaginary [Eq. (16)] parts of the Fourier transform as a function of the space coordinates η. They were recognized as the object functions described in the Fourier space and were supposed to be transformed by a 2-f system.

by the procedure before, the recorded intensities on both planes η_k $(k = 1,2)$ would be obtained numerically by

$$\widetilde{I}_k(\eta_k) = \frac{\sum_{n=1}^{N} \widetilde{I}_k(\eta_k,t_n)}{N} = \frac{\sum_{n=1}^{N} \widetilde{E}_k^*(\eta_k,t_n)\,\widetilde{E}_k(\eta_k,t_n)}{N} \quad (k = 1,2;\ n = 1,2,\ldots,N) \tag{17}$$

In the equation and also in the following paragraph, N refers to the numbers of the frames of instantaneous intensity $\widetilde{I}_k(\eta_k,t_n)$, which are to be averaged by the detector's time integration.

The recorded intensities obtained in both planes η_1 and η_2 were brought out in Fig. 3; they were the averaged results of $N = 20\,000$ frames of instantaneous intensities by Eq. (17). Figures 3(a) and 3(a′) are intensity recorded in plane η_2 before

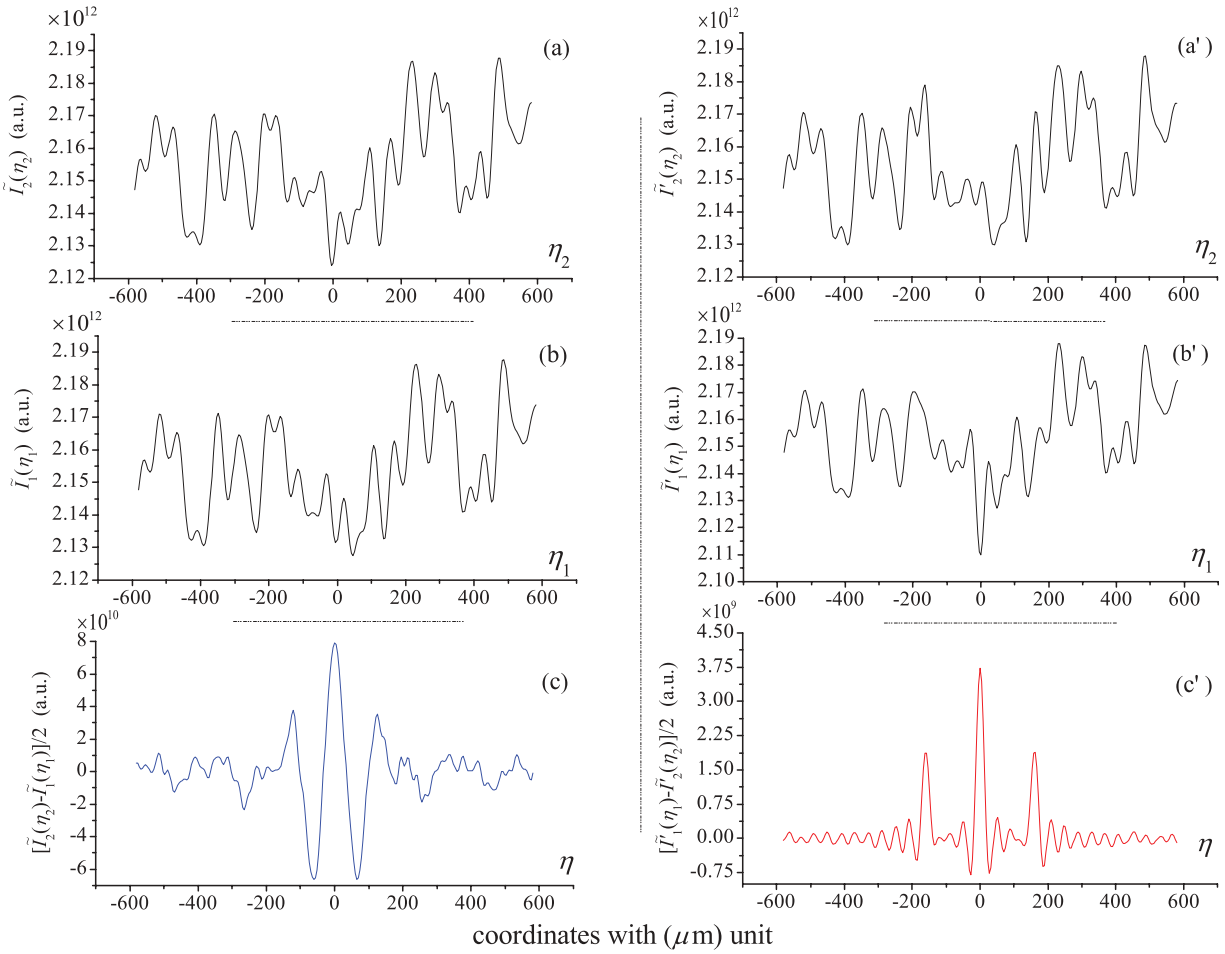

FIG. 3. (Color online) Numerical results of recorded intensity, which averaged $N = 20\,000$ frames of instantaneous intensities. The left and right columns, respectively, are related to recorded intensities before and after the phase-changing plate J of $\pi/2$ was inserted in the setup of Fig. 1. Although recorded intensities in (a) and (b) and (a′) and (b′) are in irregular appearances, their differences carried out well-defined patterns as (c) and (c′) presented. One can see, they shared the same patterns of imaginary and real parts of the conceived object in Fourier space, as Fig. 2 shows.

TABLE I. The theoretical values of parameters in Eqs. (18) and (19).

Eq. (18)		Eq. (19)	
Parameter	Theoretical value	Parameter	Theoretical value
a	$\frac{1}{2}$	a'	$2 \times \frac{105}{\lambda f} = 0.005\,26$
b	$2 \times \frac{1000}{\lambda f} = 0.050\,13$	b'	$2 \times \frac{300\pi}{\lambda f} = 0.047\,24$
c_0	0	c_1'	0
c_1	$\frac{1\,000\times 0.05}{2\pi} = 7.961\,78$	c_2'	0
c_2	$\frac{1\,000\times 0.05}{2\pi} = 7.961\,78$	p'	1
y_0	0	y_0'	0

and after the phase-changing plate J was inserted; Figs. 3(b) and 3(b′) are intensity recorded in plane η_1 before and after J was inserted; Figs. 3(c) and 3(c′) were the intensity differences between planes η_2 and η_1 obtained before and after J was inserted. We see, although intensity itself on both planes is irregular, their differences are quite well defined. Comparing Figs. 3(c′) and 3(c) with Figs. 2(a) and 2(b), the results obtained by the numerical experiment shared similar patterns of real and imaginary parts of the conceived object in Fourier space.

In Sec. VI, we quantitatively identify the obtained patterns are indeed the complex imaging of the object in Fourier space.

VI. A QUANTITATIVE COMPARISON OF THE OBJECT AND THE OBTAINED DIFFRACTION PATTERNS IN FOURIER SPACE

To compare the object and the numerically obtained diffraction patterns quantitatively, we use Eqs. (15) and (16), the object function in Fourier space, to build the nonlinear regression models. The normalized forms of them are

$$f_{\mathrm{Re}}(\eta) = \hat{y}_0 + \hat{a}[\mathrm{sinc}\,(\hat{b}\eta + \hat{c}_1) + 2\mathrm{sinc}\,(\hat{b}\eta + \hat{c}_0) + \mathrm{sinc}\,(\hat{b}\eta - \hat{c}_2)], \tag{18}$$

and

$$f_{\mathrm{Im}}(\eta) = \hat{y}_0' + \hat{p}'\,\mathrm{sinc}\,(\hat{a}'\eta + \hat{c}_1')\cos(\hat{b}'\eta + \hat{c}_2'), \tag{19}$$

where, letters with hats are parameters waiting to be estimated by the nonlinear regressions. Obviously, their theoretical values are determined by Eqs. (13), (15), and (16), as Table I shows.

With and without a phase-changing plate J inserted, the normalized form of obtained patterns, which stand for the real and the imaginary parts of the field strengths of the diffraction imaging, were obtained by the numerical experiment and were presented in Figs. 4 and 5 (scattered black squares) respectively. In both of them, each diagram of (a)–(i) is related to the situation when a sample number of instantaneous intensity for averaging is selected to be $N = 625 \times 2^n$ ($n = 0,1,\ldots,8$). Among them, the continuous lines are the fitted results with models Eqs. (18) and (19). During each fitting process shown in Figs. 4 and 5, the estimated parameters in Eqs. (18) and (19) are worked out by nonlinear regressions. They are presented in Tables II and III, correspondingly. Comparing them with parameters in Table I, we can see that the estimated parameters gradually agree with their theoretical values while N increases.

To measure how well outcomes are likely to be predicted by the models of Eqs. (18) and (19), the *coefficient of determination* (Ref. [29], p. 270) defined by $R^2 \triangleq 1 - \frac{\sum_i (\hat{y}_i - y_i)^2}{\sum_i (\hat{y}_i - \bar{y})^2}$ is investigated. (In the definition, $y_i, \bar{y}$ are obtained data and their mean values, and $\hat{y}_i$ are the model values estimated by the fitting procedure.) The values of R^2 for the fitting process related to Figs. 4(a)–4(i) and 5(a)–5(i) are listed in Tables II and III. Figure 6 presents the relations between R^2 and sample numbers N. As they showed, while N increases, R^2 was up approaching 1. The trend indicates when the N is large enough, the regression line of models Eqs. (18) and (19) would perfectly predict the data.

In order to evaluate how precisely the models agree with the obtained data, the *root-mean standard error* [defined by $\mathcal{E}_{\mathrm{RM}} \triangleq \sqrt{\frac{\sum_i (\hat{y}_i - y_i)^2}{N}}$] is also examined. The values of $\mathcal{E}_{\mathrm{RM}}$ for the fitting process related to Figs. 4(a)–4(i) and 5(a)–5(i) are also listed in Tables II and III, correspondingly. The relations between $\mathcal{E}_{\mathrm{RM}}$ and N are shown in Fig. 7. As shown, $\mathcal{E}_{\mathrm{RM}}$ was in a down trend until approaching 0 while N increased. Such a trend indicates when N is large enough, the obtained data would converge in Eqs. (18) and (19) precisely.

The comparing procedure mentioned earlier has been displayed in Figs. 4(a)–4(i) and 5(a)–5(i). Their relative data have been presented in Tables II and III. As examples, in Figs. 4(i) and 5(i), the R^2 were up to 0.998 75 and 0.9811, and

TABLE II. The estimated values $\hat{a}$, $\hat{b}$, $\hat{c}_0$, $\hat{c}_1$, $\hat{c}_2$, and $\hat{y}_0$ in Eq. (18) when $N = 625 \times 2^n$ ($n = 0,1,8$). Their corresponding theoretical values are listed in the left-hand side of Table I. The values for *the coefficient of determination* (R^2) and the *root-mean standard error* ($\mathcal{E}_{\mathrm{RM}}$) for the fitting process related to Fig. 4 are also presented in the table.

N	$\hat{a}$	$\hat{b}$	$\hat{c}_0$	$\hat{c}_1$	$\hat{c}_2$	$\hat{y}_0$	R^2	$\mathcal{E}_{\mathrm{RM}}$
625	0.527 74	0.050 44	−0.059 87	8.003 44	8.094 15	-6.5345×10^{-4}	0.865 77	0.065 56
1250	0.511 35	0.050 13	−0.052 92	8.0348	7.921 42	0.004 07	0.927 67	0.044 86
2500	0.501 85	0.050 16	−0.028 24	8.008 23	7.975 42	−0.0136	0.975 04	0.027 51
5000	0.501 12	0.050 26	−0.018 32	7.988 88	7.977 26	0.002 01	0.983 49	0.020 39
10 000	0.502 37	0.050 08	0.015 19	7.9558	7.937 13	$-8.147\,36 \times 10^{-4}$	0.988 84	0.016 72
20 000	0.513 12	0.050 22	−0.003 31	7.975 14	7.9695	−0.002 22	0.995 25	0.011 13
40 000	0.5068	0.050 18	−0.004 24	7.974 82	7.963 04	$-9.949\,32 \times 10^{-4}$	0.997 19	0.008 47
80 000	0.507 84	0.050 16	0.007 41	7.970 44	7.970 14	$-7.130\,34 \times 10^{-4}$	0.998 48	0.006 21
160 000	0.506 28	0.050 18	0.005 15	7.969 92	7.970 84	$-6.999\,92 \times 10^{-4}$	0.998 75	0.005 62

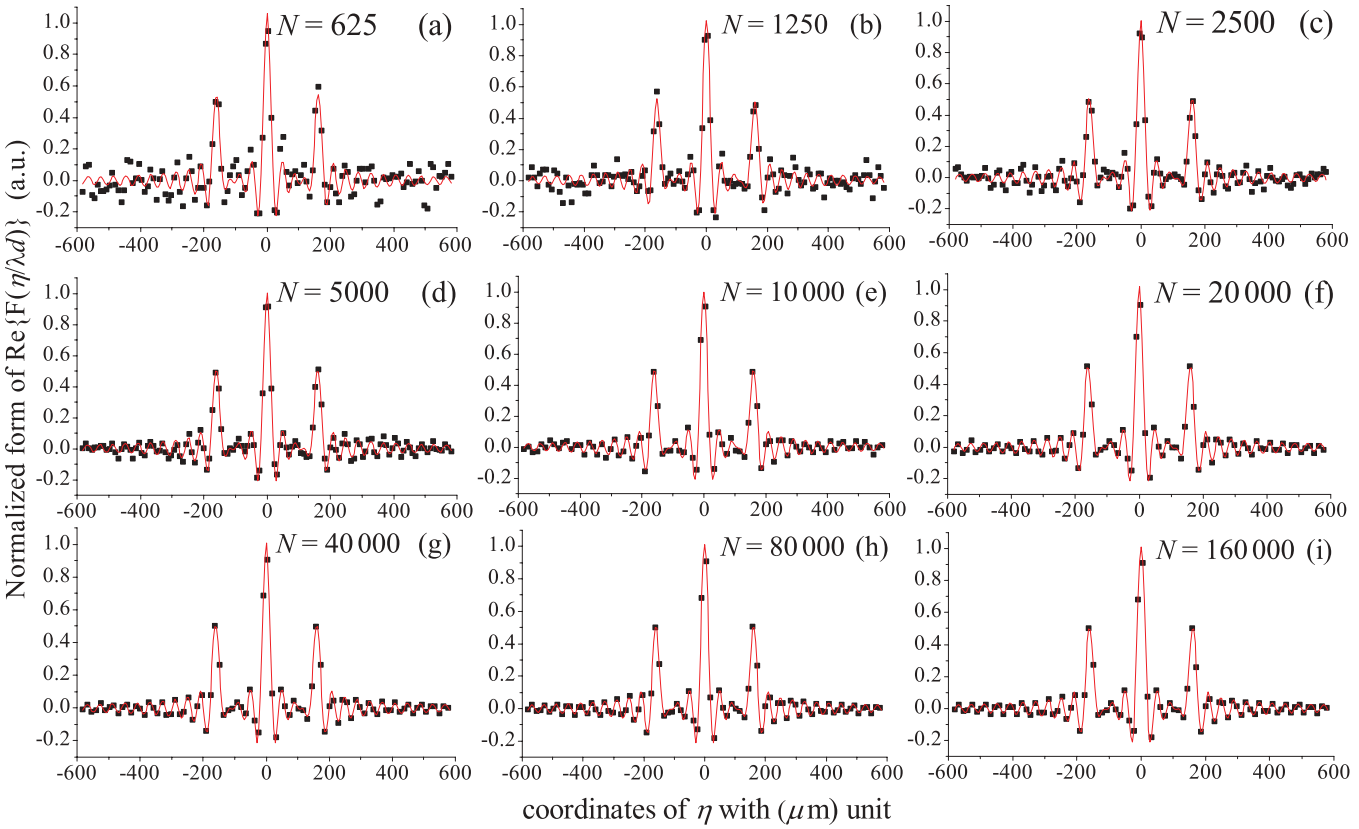

FIG. 4. (Color online) The procedure during which the obtained data converge on the models of Eq. (18). The scattered black squares are data obtained with phase-changing plate J being inserted; the continuous lines are fitted results. Diagrams from (a) to (i) are related to situations when a sample number of instantaneous intensity for averaging is $N = 625 \times 2^n$ ($n = 0,1,\ldots,8$). By using the obtained data related to each diagram, the estimated values of $\hat{a}$, $\hat{b}$, $\hat{c}_0$, $\hat{c}_1$, $\hat{c}_2$, and $\hat{y}_0$ in Eq. (18) are worked out with the use of the nonlinear regressions. They are listed in Table II with different N's. Their theoretical values are listed on the left-hand side of Table I. The *coefficient of determination* (R^2) and the *root-mean standard error* ($\mathcal{E}_{\mathrm{RM}}$) for each N are also presented in Table II; their trend lines are shown in Figs. 6(a) and 7(a).

their $\mathcal{E}_{\mathrm{RM}}$ were 0.005 62 and 0.032 79. In accord with their appearance, scattered squares and continuous lines fit almost exactly.

From the previous comparisons, we quantitatively identify that, when the number of N is large enough, the obtained diffraction patterns would precisely converge in Eqs. (18) and (19) in accord with theoretical parameters in Table I, which stand for the real and the imaginary parts of the object in Fourier space.

VII. DISCUSSIONS AND CONCLUSIONS

The patterns obtained, with and without the phase-changing plate J being inserted, are the real and the imaginary parts, respectively, of the Fraunhofer diffraction field. A theoretical derivation and a numerical example to demonstrate the acquisition procedure were presented. A quantitative comparison between the object and the obtained data is also given. They show that the real and the imaginary parts of the Fourier

TABLE III. The estimated values $\hat{a}'$, $\hat{b}'$, $\hat{c}'_1$, $\hat{c}'_2$, $\hat{p}'$, and $\hat{y}'_0$ in Eq. (19) when $N = 625 \times 2^n$ ($n = 0,1,8$). Their corresponding theoretical values are listed in the right-hand side of Table I. The values for the *coefficient of determination* (R^2) and the *root-mean standard error* ($\mathcal{E}_{\mathrm{RM}}$) for the fitting process related to Fig. 5 are also presented in the table.

N	$\hat{a}'$	$\hat{b}'$	$\hat{c}'_1$	$\hat{c}'_2$	$\hat{p}'$	$\hat{y}'_0$	R^2	$\mathcal{E}_{\mathrm{RM}}$
625	0.005 72	0.048 59	−0.249 42	−0.157 96	1.175 68	0.002 73	0.502 19	0.319 13
1250	0.0056	0.048 75	−0.202 71	0.007 4035	1.001 18	0.005 55	0.700 39	0.180 28
2500	0.005 23	0.047 75	−0.014 97	0.013 07	0.734 12	0.007 06	0.809 86	0.101 28
5000	0.0054	0.047 67	−0.021 86	−0.019 96	0.927 71	0.007 51	0.887 68	0.092 47
10 000	0.005 35	0.0476	−0.042 32	−0.0853	0.876 27	0.008 24	0.953 28	0.054 64
20 000	0.005 36	0.047 56	−0.0524	0.002 19	0.851 67	0.009 52	0.961 18	0.048 15
40 000	0.005 25	0.047 29	−0.0067	−0.009 36	0.857	0.007 29	0.9666	0.045 57
80 000	0.005 29	0.047 33	−0.017 41	0.0115	0.8373	0.0085	0.974 95	0.037 62
160 000	0.005 29	0.047 34	−0.007 65	0.002 78	0.839 25	0.0081	0.9811	0.032 79

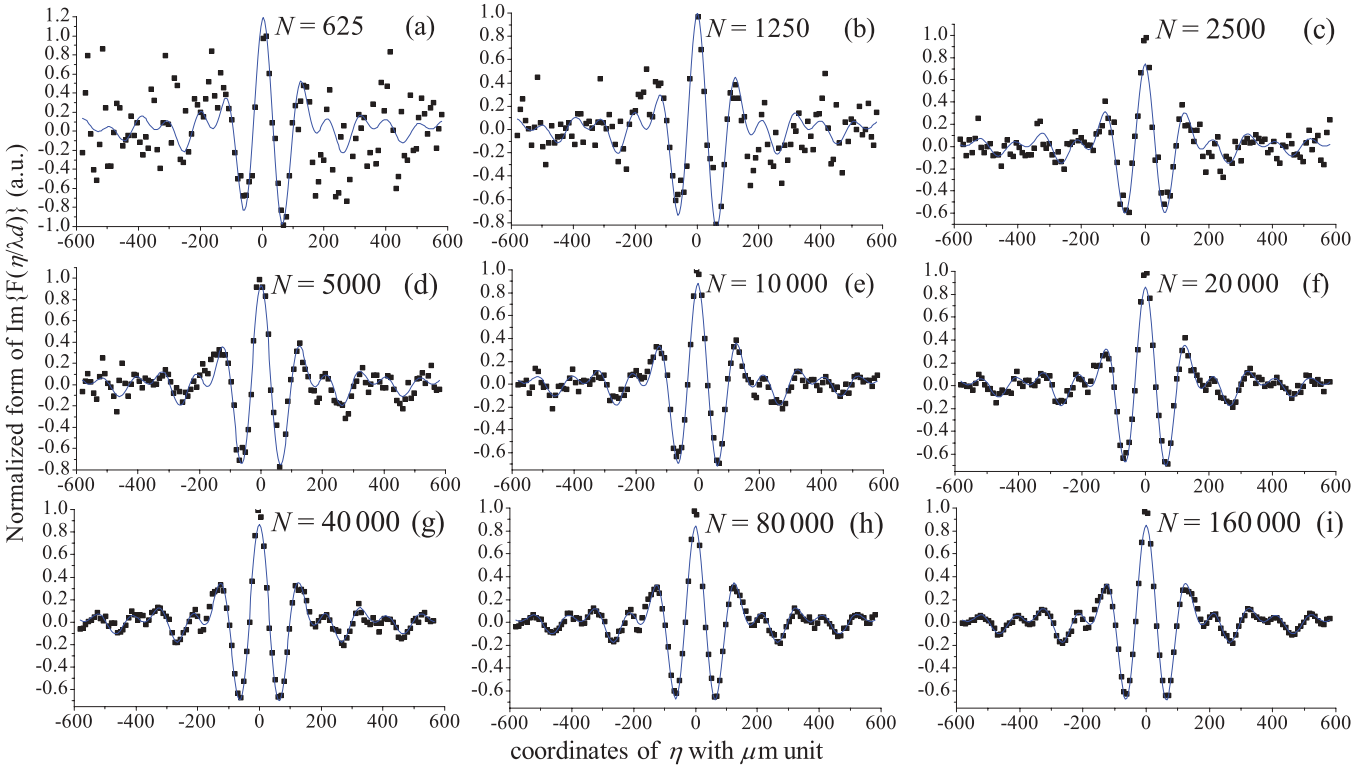

FIG. 5. (Color online) The procedure during which the obtained data converge on the models of Eq. (19). The scattered black squares are data obtained without phase-changing plate J being inserted; the continuous lines are fitted results. Diagrams from (a) to (i) are related to situations when the sample number of instantaneous intensity for averaging is $N = 625 \times 2^n$ ($n = 0,1,\ldots,8$). By using the obtained data related to each diagram, the estimated values of $\hat{a}'$, $\hat{b}'$, $\hat{c}_1'$, $\hat{c}_2'$, $\hat{p}'$, and $\hat{y}_0'$ in Eq. (19) are worked out with the use of the nonlinear regressions; they are listed in Table III with different N's. Their corresponding theoretical values are listed in the right-hand side of Table I. The *coefficient of determination* (R^2) and the *root-mean standard error* ($\mathcal{E}_{\mathrm{RM}}$) for each N are also presented in Table III; their trend lines are shown in Figs. 6(b) and 7(b).

transform of a conceived object were both retrieved in good agreement with theoretical anticipation. The whole process is a pure physical procedure needing no iterative algorithms and without a support constraint. The aim of this paper is to determine the basic problem of the phases of the diffracted beams. The theory may also apply equally to those situations, such as synchrotron radiation hard x-ray imaging [30] and neutron-diffraction tomography [31,32], where high intensity and a highly brilliant coherent source were difficult to attain. The importance of such issues had been discussed, in detail, in Ref. [13].

The mechanisms behind the proposed setup to obtain the diffraction patterns are quite different from the Mach-Zehnder interferometer. In the latter, the observed fringes were caused by the first-order coherence of the light. That requires coherent illumination. In the work of this paper, the fringes obtained

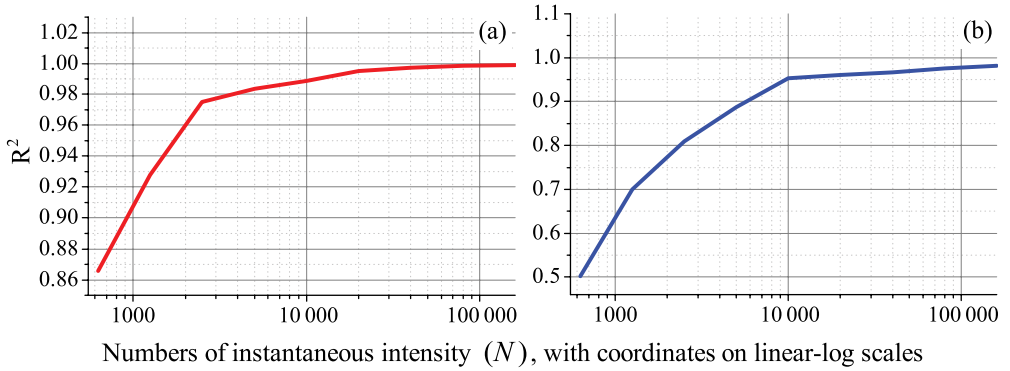

FIG. 6. (Color online) Relations between the *coefficient of determination* (R^2) and the sample numbers N. As shown, R^2 was in an up trend while approaching 1. This indicates when N is large enough, the regression models Eqs. (18) and (19) would perfectly predict the data. (a) The trend line of $R^2 - N$ for the retrieval process of Fig. 4; (b) The trend line of $R^2 - N$ for the retrieval process of Fig. 5.

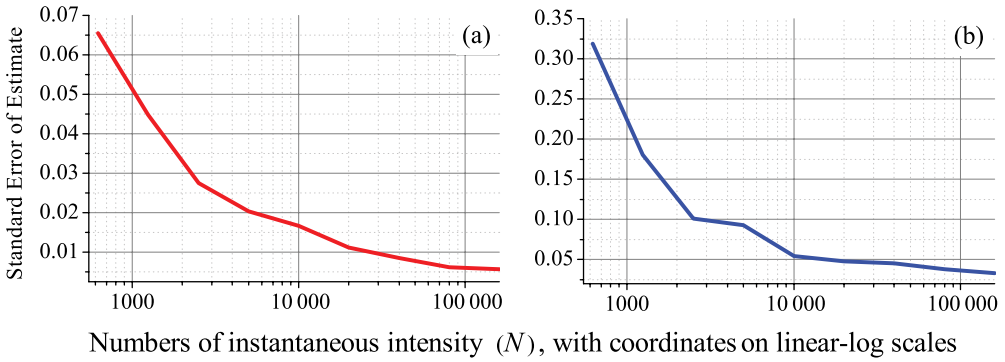

FIG. 7. (Color online) The relations between the *root-mean standard error* ($\mathcal{E}_{\mathrm{RM}}$) and the sample numbers N. As shown, $\mathcal{E}_{\mathrm{RM}}$ was in a down trend while approaching 0. This indicates when N is large enough, the obtained data would converge in the regression models Eqs. (18) and (19) precisely. (a) The trend line of $\mathcal{E}_{\mathrm{RM}\text{-}N}$ for the retrieval process of Fig. 4; (b) The trend line of $\mathcal{E}_{\mathrm{RM}\text{-}N}$ for the retrieval process of Fig. 5.

were caused by mutual correlation of the fields, and no coherent source was needed, as Eqs. (5) and (6) indicate. That is the key difference. In fact, there had been previous work concerned with measuring the mutual coherence function through interferometry [33].

The reason we use deflection and rotation devices (L and M) rather than plane mirrors to guide the optical path is that such an arrangement leads Eq. (13) to exist. If we used plane mirrors as used in Mach-Zehnder interferometer, Eq. (13) would have been $\eta_1 = \eta_2$, and Eq. (6) would become a constant value, therefore, the fringes would not be observed. The appearance of such kinds of fringes can be explained intuitively by Klyshko's advanced wave-interference theory [34]. Equation (6) can be interpreted as a scenario of the impinging of two conjugate and backward wave fronts of $E(\eta_1)$ and $E(\eta_2)$, hence, canceling the spherical part of the wave fronts and remaining the only plane-wave front to compose a Fourier transform.

The beam splitter BS_2 introduces a π phase shift upon reflecting from the upper side, but introduces no phase shifts upon reflection on the lower side and on transmission in any side. Without these characteristics, the approach will not work. It is well known that such a nature can be achieved by optical filming techniques.

To the best of our knowledge, it was the first physical proposal for the complex acquisition of the two-dimensional diffraction field with quasimonochromatic incoherent light. Yet a solution of the phase problem in the theory of structure determination of crystals from x-ray diffraction experiments with coherent illumination was also suggested by Wolf very recently [35]. The feasibility of obtaining the fringes by incoherent light via intensity distribution rather than by coincident rate or intensity correlation function was discussed not long ago and has been verified experimentally [36].

As we have compared in Fourier space, the obtained data would converge upon the function of objects as the number of N increases. Since N can be viewed as the amount of instantaneous intensity to be averaged due to the detectors' time integral, the precise imaging may benefit from the slow responding detectors.

Finally, we mention our suggested scheme differs from vast literature on getting phase information with white-light interferometry. The latter obtains information from the time-frequency domain. Also, it is fundamentally different from incoherent holography. Their differences are illustrated in Ref. [36].

ACKNOWLEDGMENTS

M.Z. is supported by the Project 211 Foundation of Anhui University (Grant No. 02203104). Q.W. is supported by National Natural Science Foundation of China (Grant No. 60877009). The authors thank the anonymous referee for his helpful comments.

[1] V. Elser, J. Opt. Soc. Am. A **20**, 40 (2003).
[2] J. R. Fienup, Opt. Lett. **3**, 27 (1978).
[3] S. Marchesini, Rev. Sci. Instrum. **78**, 011301 (2007).
[4] J. R. Fienup, J. Opt. Soc. Am. A **4**, 118 (1987).
[5] S. Marchesini and C. S. Fadley, Phys. Rev. B **67**, 024115 (2003).
[6] J. Cheng and S. Han, J. Opt. Soc. Am. A **18**, 1460 (2001).
[7] G. J. Williams, M. A. Pfeifer, I. A. Vartanyants, and I. K. Robinson, Phys. Rev. Lett. **90**, 175501 (2003).
[8] J. Miao, T. Ishikawa, B. Johnson, E. H. Anderson, B. Lai, and K. O. Hodgson, Phys. Rev. Lett. **89**, 088303 (2002).
[9] I. K. Robinson, I. A. Vartanyants, G. J. Williams, M. A. Pfeifer, and J. A. Pitney, Phys. Rev. Lett. **87**, 195505 (2001).
[10] J. W. Miao *et al.*, Nature (London) **400**, 342 (1999).
[11] J. Miao, D. Sayre, and H. N. Chapman, J. Opt. Soc. Am. A **15**, 1662 (1998).
[12] J. Miao *et al.*, Annu. Rev. Phys. Chem. **59**, 387 (2008).
[13] M. Zhang *et al.*, Phys. Rev. A **75**, 021803(R) (2007).
[14] J. Xiong, D.-Z. Cao, F. Huang, H.-G. Li, X.-J. Sun, and K. Wang, Phys. Rev. Lett. **94**, 173601 (2005).
[15] J. Cheng and S. S. Han, Phys. Rev. Lett. **92**, 093903 (2004).

[16] Y.-H. Zhai, X.-H. Chen, D. Zhang, and L.-A. Wu, Phys. Rev. A **72**, 043805 (2005).
[17] G. Scarcelli, A. Valencia, and Y. Shih, Europhys. Lett. **68**, 618 (2004).
[18] M. Bache, D. Magatti, F. Ferri, A. Gatti, E. Brambilla, and L. A. Lugiato, Phys. Rev. A **73**, 053802 (2006).
[19] M. Zhang *et al.*, Phys. Lett. A **366**, 569 (2007).
[20] G. Ying *et al.*, Opt. Commun. **281**, 5130 (2008).
[21] J. Miao, J. Kirz, and D. Sayre, Acta Crystallogr., Sect. D: Biol. Crystallogr. **56**, 1312 (2000).
[22] J. M. Rodenburg, A. C. Hurst, A. G. Cullis, B. R. Dobson, F. Pfeiffer, O. Bunk, C. David, K. Jefimovs, and I. Johnson, Phys. Rev. Lett. **98**, 034801 (2007).
[23] R. Borghi, F. Gori, and M. Santarsiero, Phys. Rev. Lett. **96**, 183901 (2006).
[24] M. Born and E. Wolf, *Principles of Optics*, 7th (expanded) ed. (Cambridge University Press, Cambridge, UK, 1999).
[25] J. W. Goodman, *Introduction to Fourier Optics*, 2nd ed. (McGraw-Hill, CO, New York, 1998).
[26] J. W. Goodman, *Statistical Optics* (Wiley, Hoboken, NJ, 2000).
[27] An optical system composed of one lens with both focal planes. When the object was illuminated with coherent light in the front focal plane, the field strength existing in the rear focal plane would be the Fourier transform of the object. (See also, Ref. [25], pp. 104–105.)
[28] M. Zhang *et al.*, Acta Opt. Sin. **27**, 1858 (2007).
[29] M. R. Spiegel, J. J. Schiller, and R. A. Srinivasan, *Probability and Statistics* (McGraw-Hill, New York, 2009).
[30] M. Jiang *et al.*, Chin. Sci. Bull. **54**, 4171 (2009).
[31] B. Sur *et al.*, Nature (London) **414**, 525 (2001).
[32] B. Sur, R. B. Rogge, R. P. Hammond, V. N. P. Anghel, and J. Katsaras, Phys. Rev. Lett. **88**, 065505 (2002).
[33] J. B. Breckinridge, J. Opt. Soc. Am. **65**, 755 (1975).
[34] D. N. Klyshko, Phys. Lett. A **128**, 133 (1988).
[35] E. Wolf, Phys. Rev. Lett. **103**, 075501 (2009).
[36] S.-H. Zhang, L. Gao, J. Xiong, L.-J. Feng, D.-Z. Cao, and K. Wang, Phys. Rev. Lett. **102**, 073904 (2009).